Monthly Notices
of the
ROYAL ASTRONOMICAL SOCIETY
MNRAS **442,** 3777–3790 (2014) doi:10.1093/mnras/stu1139

The effect of accretion on the measurement of neutron star mass and radius in the low-mass X-ray binary 4U 1608−52

Juri Poutanen,[1,2]★ Joonas Nättilä,[1,2] Jari J. E. Kajava,[2,3,4] Outi-Marja Latvala,[2] Duncan K. Galloway,[5,6] Erik Kuulkers[3] and Valery F. Suleimanov[7,8]

[1]*Tuorla Observatory, University of Turku, Väisäläntie 20, FI-21500 Piikkiö, Finland*
[2]*Astronomy Division, Department of Physics, PO Box 3000, FI-90014 University of Oulu, Finland*
[3]*European Space Astronomy Centre (ESA/ESAC), Science Operations Department, E-28691 Villanueva de la Cañada, Madrid, Spain*
[4]*Nordic Optical Telescope, Apartado 474, E-38700 Santa Cruz de La Palma, Spain*
[5]*Monash Centre for Astrophysics (MoCA), Monash University, Clayton, VIC 3800, Australia*
[6]*School of Physics and School of Mathematical Sciences, Monash University, Clayton, VIC 3800, Australia*
[7]*Institut für Astronomie und Astrophysik, Kepler Centre for Astro and Particle Physics, Universität Tübingen, Sand 1, D-72076 Tübingen, Germany*
[8]*Astronomy Department, Kazan (Volga region) Federal University, Kremlyovskaya str. 18, 420008 Kazan, Russia*

Accepted 2014 June 6. Received 2014 June 6; in original form 2014 May 8

ABSTRACT

Spectral measurements of thermonuclear (type I) X-ray bursts from low-mass X-ray binaries have been used to measure neutron star (NS) masses and radii. A number of systematic issues affect such measurements and have raised concerns as to the robustness of the methods. We present analysis of the X-ray emission from bursts observed from 4U 1608−52 at various persistent fluxes. We find a strong dependence of the burst properties on the flux and spectral hardness of the persistent emission before burst. Bursts occurring during the low accretion rate (hard) state exhibit evolution of the blackbody normalization consistent with the theoretical predictions of NS atmosphere models. However, bursts occurring during the high accretion rate (soft) state show roughly constant normalization, which is inconsistent with the NS atmosphere models and therefore these bursts cannot be easily used to determine NS parameters. We analyse the hard-state burst to put the lower limit on the NS radius R in 4U 1608−52 of 12 km (for masses 1.0–2.4 $M_\odot$). We constrain R to be between 13 and 16 km for masses 1.2–1.6 $M_\odot$. The best agreement with the theoretical NS mass–radius relations is achieved for source distances in the range 3.1–3.7 kpc. We expect that the radius limit will be 10 per cent lower if spectral models including rapid rotation are used instead.

Key words: stars: atmospheres – stars: neutron – X-rays: bursts – X-rays: individual: 4U 1608−52.

1 INTRODUCTION

Neutron stars (NS) are among the most compact observable objects in our Universe. Their core densities can exceed the nuclear density by a factor of 2–5. This makes them interesting testbeds of physics under extreme conditions practically unattainable in the terrestrial laboratories. However, this also means that the equation of state (EoS) of supranuclear matter has large uncertainties, because laboratory measurements are difficult (Lattimer & Prakash 2007) and computations from first principles are practically impossible, because of the extreme complexity of multibody nucleon interactions (e.g. Chamel et al. 2013).

Measuring NS masses and radii using astronomical observations offers a way to constrain the EoS (Haensel, Potekhin & Yakovlev 2007; Lattimer & Prakash 2007; Lattimer 2012). Recent observations of 2 $M_\odot$ pulsars (Demorest et al. 2010; Antoniadis et al. 2013) appear to disfavour the softest EoS. Better constraining the EoS from observations, however, requires not only the mass, but also the radius to be determined. In principle, constraints on the radii can be obtained from the measurements of the moment of inertia, but it is a difficult task that might take decades to complete even in the most relativistic system known (Lyne et al. 2004; O'Connell 2004; Lattimer & Schutz 2005; Kramer & Stairs 2008). Thermal emission from NS potentially offers a better tool to measure their radii. Cooling NS in quiescent low-mass X-ray binaries (LMXBs) situated in globular clusters with known distances allow one to determine their apparent radii, but not masses and radii independently. The major problem here is that these measurements give very different,

★ E-mail: juri.poutanen@utu.fi

mutually excluding radii for different objects (Guillot et al. 2013), and the results depend heavily on the assumed chemical composition and the value of the interstellar absorption (Lattimer & Steiner 2014b). The available data offer basically one snapshot for each object and do not allow thorough tests of the models, for example, by checking the consistency between the observed spectral evolution and the theory.

X-ray bursters can provide tighter constraints on the mass–radius relation (e.g. Damen et al. 1990; van Paradijs et al. 1990; Lewin, van Paradijs & Taam 1993). First, the so-called photospheric radius expansion (PRE) bursts are powerful enough to exceed the Eddington limit (Grindlay et al. 1980; Lewin, Vacca & Basinska 1984; Tawara, Hayakawa & Kii 1984), which therefore can be potentially measured (see Kuulkers et al. 2003). Secondly, cooling of the NS surface during the burst provides a large set of time-resolved spectra, which allow measurement of the apparent NS radius at different fluxes. Furthermore, each object typically shows many bursts which can be used for consistency checks. If the distance to the source is known, then these observations in principle allow constraints on both the mass and the radius.

A serious problem encountered with this approach is that the distances are not known with sufficient accuracy, resulting in large error boxes elongated along the curve of constant Eddington temperature [see equation (A8) in Appendix A], which is distance independent (Suleimanov et al. 2011b). On the other hand, some of the reported measurements (Özel, Güver & Psaltis 2009; Güver et al. 2010a,b) give no solutions for mass and radius for most of the parameter space resulting in mass–radius constraints much more accurate than the distance error would allow. This casts doubts on the whole approach (Steiner, Lattimer & Brown 2010). Another problem is that the radii determined from different objects turned out to be very different, depending on the applied method (the touchdown or the cooling tail approach) and the bursts selected for the analysis (see Suleimanov et al. 2011b). The most alarming is a clear dependence of the measured apparent radii on the accretion state of the object where the burst occurs, as was shown for the case of 4U 1724−307 by Suleimanov et al. (2011b). A more extended recent study of Kajava et al. (2014) demonstrated that X-ray burst cooling properties in 11 LMXBs are dependent on the accretion rate and the spectral state.

In this paper, we concentrate on 4U 1608−52 which shows PRE bursts over a wide range of persistent fluxes, and in different spectral states. This allows us to study the cooling of the bursts at different mass accretion rates. The aim of this study is to understand, using 4U 1608−52 as an example, which kind of bursts evolve according to the available theoretical models, and how the difference in the cooling tail behaviour impacts the NS mass and radius measurements.

2 PRE X-RAY BURSTS FROM 4U 1608−52

2.1 The companion and the distance to 4U 1608−52

To the best of our knowledge, there are no spectroscopic measurements of the optical counterpart QX Nor to LMXB 4U 1608−52. However, Wachter et al. (2002) have detected periodic variability at the time-scale of 0.537 d, which they have attributed to the superhump period, which is very close to the orbital period of the system (Kato, Fukue & Mineshige 1998). Observations of QX Nor in quiescence indicate an F to G main-sequence secondary, while theoretical arguments are in favour of an evolved donor (Wachter et al. 2002). In either case, the companion is likely to be a hydrogen-rich star.

4U 1608−52 does not reside in any known globular cluster making distance to the source hard to measure. Nevertheless, there have been several estimates by different authors using various methods. Using X-ray bursts, Ebisuzaki (1987) obtained a distance $D = 3.8 \pm 0.4$ kpc by fitting a theoretical model to the observed dependence of the colour temperature on luminosity. Nakamura et al. (1989) gave a distance of 3.6 kpc based on comparison between the Eddington limit for helium-rich envelope and the most luminous PRE burst observed at the time. Galloway et al. (2008) derived a distance of 3.2 ± 0.3 or 4.1 ± 0.4 kpc from the peak fluxes of the PRE bursts assuming solar composition or helium, respectively. More recent measurements have been made by Güver et al. (2010a) who obtained $D = 5.8^{+2.0}_{-1.9}$ kpc with a lower cutoff at 3.9 kpc, based on the study of the interstellar extinction towards the source. To cover all possibilities, we assume a Gaussian distribution of distances with a mean of 5.8 kpc and a standard deviation of 2 kpc on both sides. We will also highlight what is the effect of having the cutoff at 3.9 kpc on the *M*–*R* constraints in Sections 3.2 and 3.3.

2.2 Data

The data covering 2.5–25 keV range from the Proportional Counter Array (PCA; Jahoda et al. 2006) spectrometer on board the *Rossi X-ray Timing Explorer* (*RXTE*) were analysed with the HEASOFT package (version 6.11.1), and response matrices were generated using PCARSP (11.7.1). The backgrounds of PCA detectors were estimated with `CM_bright_VLE` model and all the spectral data were fitted using XSPEC 12.8.1g package (Arnaud 1996), assuming a recommended 0.5 per cent systematic error (Jahoda et al. 2006). In order to take low count rate bins into account, we also adopted Churazov weighting (Churazov et al. 1996). All error limits were obtained using the `error` task in XSPEC with 1σ confidence levels.

We analysed all publicly available *RXTE* data from 1995 December 30 through 2012 January 5. During this time *RXTE* observed 56 bursts from 4U 1608−52 of which 21 were recognized as PRE bursts. Time-resolved spectra for the bursts were then extracted using an initial integration time of 0.25 s. Then each time the count rate after the peak decreased by a factor of $\sqrt{2}$ the integration time was doubled. The exposure for each time bin was corrected for the dead time following the approach recommended by the instrument team.[1] It resulted in a roughly 10–15 per cent increase in the peak flux, with the difference decreasing quickly as the observed flux drops. A spectrum extracted from a 16 s period prior to the burst was then subtracted as the background for each burst (Kuulkers et al. 2002, and references therein). We checked that the difference in burst characteristics with and without background subtraction is negligible at least at high burst fluxes (at $F > 0.2\,F_{\rm td}$). We also note that variations in the persistent emission during the burst are in principle possible. However, in the cooling tail of the bursts, they are less significant and the observed distribution of the deviations in the persistent level is very similar to the simulated distribution where no variation was assumed (see figs 4, 6 and 7 in Worpel, Galloway & Price 2013). In any case, these variations cannot significantly affect the spectral characteristics because most bursts occur at the persistent flux level below a few per cent of the burst peak flux (see Table 1).

Because the burst spectra are known to be well described by the blackbody (Lewin et al. 1993) and to make easy comparison with previous studies, we fit these dead-time-corrected spectra with

[1] http://heasarc.gsfc.nasa.gov/docs/xte/recipes/pca_deadtime.html

Table 1. PRE X-ray bursts from 4U 1652−08.

No.[a]	ID[b]	Start time[c]	$F_{\rm td,-9}$ [d]	$E_{\rm tot,-6}$ [e]	$E_{\rm td,-6}$ [f]	$\tau_{\rm td}$ [g]	$F_{\rm per,-9}$ [h]	$K_{\rm td/2}/K_{\rm td}$ [i]	S_z [j]
1	30062-01-01-00	50899.58793	195 ± 3	1.67 ± 0.01	0.721 ± 0.004	3.50 ± 0.38	2.94 ± 0.03	1.1 ± 0.1	2.0
2	30062-01-02-05	50914.27554	127 ± 2	1.62 ± 0.01	0.720 ± 0.003	6.25 ± 0.13	0.94 ± 0.02	3.1 ± 0.2	2.0
3	50052-02-01-01	51612.03172	145 ± 4	1.05 ± 0.01	0.476 ± 0.005	4.25 ± 0.13	1.47 ± 0.04	1.7 ± 0.3	2.2
4	50052-01-04-00	51614.07214	125 ± 3	1.98 ± 0.01	0.973 ± 0.004	7.75 ± 0.25	0.74 ± 0.02	3.8 ± 0.3	1.5
5	70059-01-08-00	52499.40489	107 ± 2	0.65 ± 0.01	0.234 ± 0.002	3.75 ± 0.13	13.74 ± 0.05	1.4 ± 0.1	2.6
6	70059-01-20-00	52524.10246	181 ± 4	1.44 ± 0.01	0.512 ± 0.004	3.50 ± 0.13	5.13 ± 0.09	1.0 ± 0.1	2.2
7	70059-01-21-00	52526.16094	154 ± 2	1.87 ± 0.01	0.565 ± 0.005	3.25 ± 0.38	6.79 ± 0.03	1.1 ± 0.1	2.3
8	70059-03-01-00	52529.18022	178 ± 7	2.32 ± 0.01	0.683 ± 0.005	3.50 ± 0.25	4.34 ± 0.04	1.0 ± 0.2	2.1
9	70058-01-39-00	52536.31811	169 ± 2	1.35 ± 0.01	0.481 ± 0.003	3.75 ± 0.38	2.51 ± 0.03	1.6 ± 0.1	2.2
10	70069-01-01-00	52542.50168	141 ± 3	2.19 ± 0.01	1.038 ± 0.004	7.75 ± 0.50	0.66 ± 0.02	3.5 ± 0.3	1.7
11	70059-01-26-00	52546.90031	126 ± 4	1.68 ± 0.01	0.705 ± 0.005	5.75 ± 0.13	0.74 ± 0.02	3.3 ± 0.3	1.9
12	80406-01-04-08	52727.18614	150 ± 3	3.28 ± 0.01	1.851 ± 0.006	13.5 ± 1.0	0.60 ± 0.02	3.4 ± 0.2	0.7
13	90408-01-04-04	53104.40883	128 ± 6	1.93 ± 0.01	0.834 ± 0.004	7.25 ± 0.13	0.89 ± 0.02	3.4 ± 0.4	1.4
14	93408-01-23-02	54434.97422	172 ± 4	1.58 ± 0.01	0.688 ± 0.004	4.00 ± 0.13	3.36 ± 0.05	1.3 ± 0.2	2.2
15	93408-01-25-06	54452.11635	109 ± 4	1.98 ± 0.01	0.438 ± 0.003	5.00 ± 0.13	1.66 ± 0.02	3.9 ± 0.3	0.8
16	93408-01-26-04	54461.03140	120 ± 3	2.25 ± 0.01	0.681 ± 0.003	6.50 ± 0.13	1.62 ± 0.02	4.8 ± 0.4	0.8
17	93408-01-59-03	54692.07545	124 ± 4	2.07 ± 0.01	0.965 ± 0.004	7.75 ± 0.13	0.67 ± 0.02	3.8 ± 0.3	1.8
18	94401-01-25-02	54997.68024	104 ± 3	0.78 ± 0.01	0.311 ± 0.004	3.50 ± 0.25	1.70 ± 0.03	1.4 ± 0.3	2.0
19	95334-01-03-08	55270.22105	170 ± 5	1.71 ± 0.01	0.617 ± 0.004	3.75 ± 0.13	6.34 ± 0.05	1.3 ± 0.2	2.1
20	96423-01-11-01	55725.15591	166 ± 3	1.81 ± 0.01	0.575 ± 0.003	3.25 ± 0.13	4.91 ± 0.04	0.9 ± 0.1	2.2
21	96423-01-35-00	55890.37147	112 ± 3	2.92 ± 0.01	1.333 ± 0.006	10.50 ± 0.25	1.55 ± 0.04	4.1 ± 0.4	0.9

[a]Burst number.
[b]Observation ID during which the burst was observed.
[c]Burst start time in MJD.
[d]Touchdown flux in units of 10^{-9} erg cm^{-2} s^{-1}.
[e]Burst fluence in units of 10^{-6} erg cm^{-2}.
[f]Burst fluence from the burst start until the touchdown in units of 10^{-6} erg cm^{-2}.
[g]Time from the beginning of the burst to the touchdown (s).
[h]Persistent (unabsorbed) flux level (in the interval 2.5–25 keV) prior to the burst in units of 10^{-9} erg cm^{-2} s^{-1}.
[i] *K*-ratio, i.e. the ratio of the blackbody normalizations at 1/2 of the touchdown flux to that at the touchdown.
[j]Value of S_z of the object on the colour–colour diagram before the burst, $S_z \lesssim 2$ corresponds to the low hard state, while $S_z \gtrsim 2$ is in the high soft state.

a blackbody model BBODYRAD affected by interstellar absorption (model PHABS). The obtained parameters are then compared to the predictions of the atmosphere models. For the hydrogen column density, we adopt the value $N_{\rm H} = 8.9 \times 10^{21}$ cm^{-2} obtained from the *BeppoSAX* observations of 4U 1608−52 (Keek et al. 2008). The best-fitting parameters are the blackbody (colour) temperature $T_{\rm bb}$ and the normalization constant $K \equiv (R_{\rm bb}[{\rm km}]/D_{10})^2$, where $D_{10} = D/10$ kpc. The time-resolved spectral parameters of analysed PRE bursts are shown in Fig. 1.

These bursts show typical characteristics of PRE: fast rise of the flux at the beginning and peak in the normalization after a few seconds. The temperature evolution of these bursts also shows the characteristic double-peaked structure, arising from the cooling of the photosphere when it expands and the subsequent heating when it collapses back towards the surface. Because of this expansion, we can assume that the flux has reached the Eddington limit. The moment when the temperature reaches its second peak and normalization its minimum is defined to be the touchdown (but see Steiner et al. 2010), where the atmosphere has collapsed back to the NS surface (due to the data gaps during burst 12, the touchdown was defined there to be just before the gap). This also marks the beginning of the cooling phase where normalization rises to a nearly constant level while the flux and the temperature continue to decrease for the rest of the burst.

From the flux evolution, we have determined different characteristics of the bursts such as the touchdown flux, the total burst fluence, the burst fluence until the touchdown and the time from the beginning of the burst to the touchdown. For every PRE burst, we have obtained the dead-time-corrected spectrum of the persistent emission using 160 s long interval just before the burst. These spectra were then fitted with a model consisting of a blackbody (BBODYRAD), Comptonization (COMPTT) component (Titarchuk 1994) and an iron line with the energy fixed at 6.4 keV, attenuated by interstellar absorption (PHABS). The observed source flux over the energy range 2.5–25 keV was estimated using the CFLUX model of XSPEC. In order to characterize the persistent spectrum before the bursts, we also computed hard and soft X-ray colours as the ratio of fluxes in the (8.6–18.0)/(5.0–8.6) and (3.6–5.0)/(2.2–3.6) keV energy bands (see Fig. 2). From these colours, we were able to define the S_z coordinate locus using a similar method as in Galloway et al. (2008). The S_z is thought to be related to mass accretion rate but the exact dependence is not known (van der Klis 1995). The spectra of the persistent emission are presented in Fig. 3. We have separated them into two groups depending the value of S_z and the shape of the spectrum: the left-hand panel shows the spectra with $S_z \lesssim 2$ (hard state), while the right-hand panel is for $S_z \gtrsim 2$ (soft state). All obtained parameters and associated 1σ errors are listed in Table 1.

In addition to the PRE bursts observed by *RXTE*, we have used the time-resolved X-ray spectral fits of two exceptional bursts observed by *EXOSAT*/ME in 1984 July 5 and 1986 March 12 during the hard state and a very low persistent flux (Gottwald et al. 1987; Penninx et al. 1989).

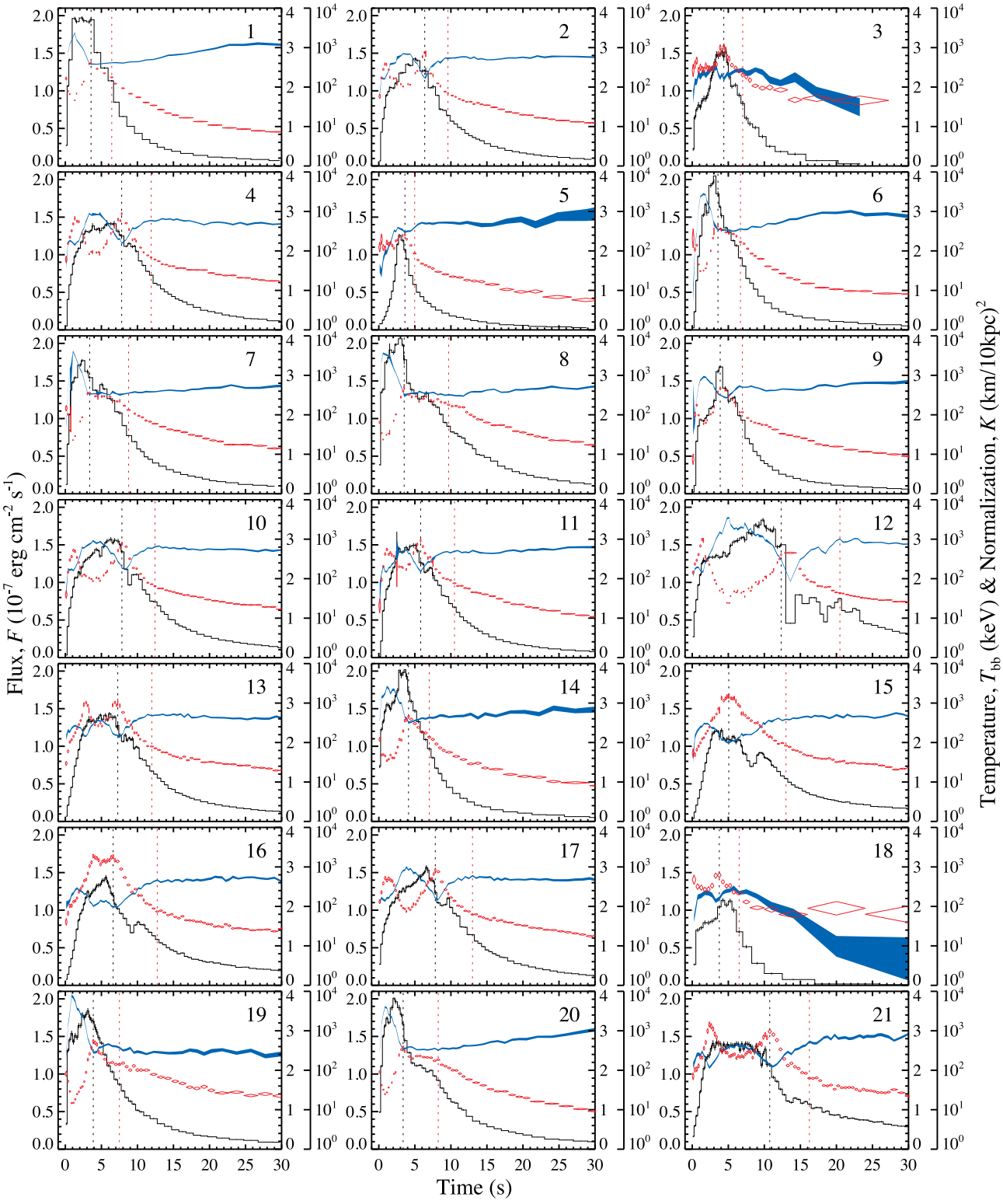

Figure 1. Flux, temperature and blackbody radius evolution during PRE bursts. The black line in each panel shows the bolometric flux (left-hand y-axis). The blue ribbon shows the 1σ limits of the normalization (outer right-hand y-axis). The red diamonds correspond to the 1σ error box for blackbody temperature (inner right-hand y-axis). Blue and red vertical dotted lines mark the touchdown and the time when the flux dropped to half the touchdown value, respectively.

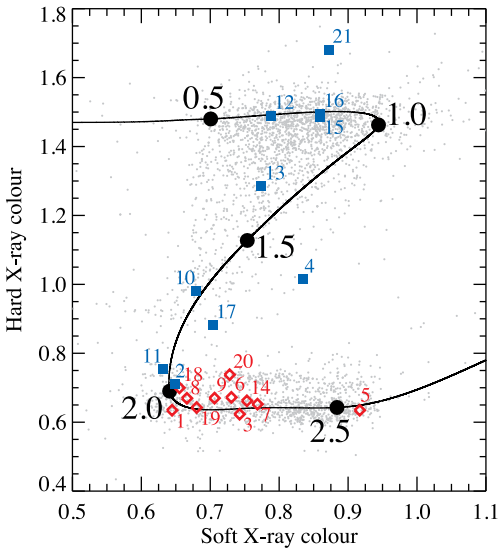

Figure 2. Colour–colour diagram showing the S_z parameter locus of the persistent spectrum before each PRE burst. The positions of the hard-state bursts are marked with blue squares and soft-state bursts with red diamonds. The burst numbering follows Table 1. Grey dots show the positions of the object as determined from the data taken in 160 s long intervals.

3 RESULTS

3.1 Burst spectral evolution and its relation to the persistent emission

Spectral evolution of the bursts during the cooling tail contains the information about NS compactness. It is this part of the burst that should be compared to theoretical models of NS atmospheres in order to constrain the mass and radius using the cooling tail method (see Appendix A and Suleimanov, Poutanen & Werner 2011a for a full description of the method). Important assumptions of the method are that during the cooling tail there are no eclipses of the NS and that the net burst spectrum is formed in a passively cooling NS atmosphere (i.e. not influenced by the accretion flow). In that case, the theory predicts that $K^{-1/4}$ is proportional to the colour-correction factor f_c, which falls from a value exceeding 1.8 at the touchdown when $L \approx L_{\rm Edd}$ to $f_c \lesssim 1.5$ at $L \approx 0.5 L_{\rm Edd}$ (Suleimanov et al. 2011a, 2012). If the Eddington luminosity is reached near the touchdown, the ratio of observed blackbody normalizations at half the touchdown flux to that at the touchdown $K_{\rm td/2}/K_{\rm td}$ (which we will call the K-ratio) should exceed 2 (just because $f_c(L_{\rm Edd})/f_c(L_{\rm Edd}/2) \gtrsim 1.2$). The data, however, show a clear dependence of the K-ratio on the value of S_z (see Fig. 4a), with a number of bursts having $K_{\rm td/2}/K_{\rm td} < 2$. It also depends on other model-independent

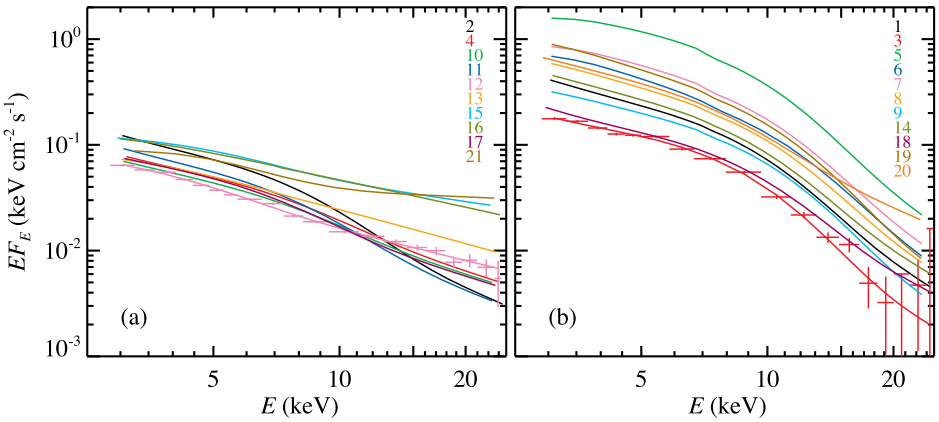

Figure 3. Model spectra of the persistent emission before each PRE burst (a) for $S_z \lesssim 2$ (low hard state) and (b) for $S_z \gtrsim 2$ (high soft state). The unfolded spectrum for one event is shown by crosses in each panel. The burst numbering follows Table 1 and colours are used only for easier identification.

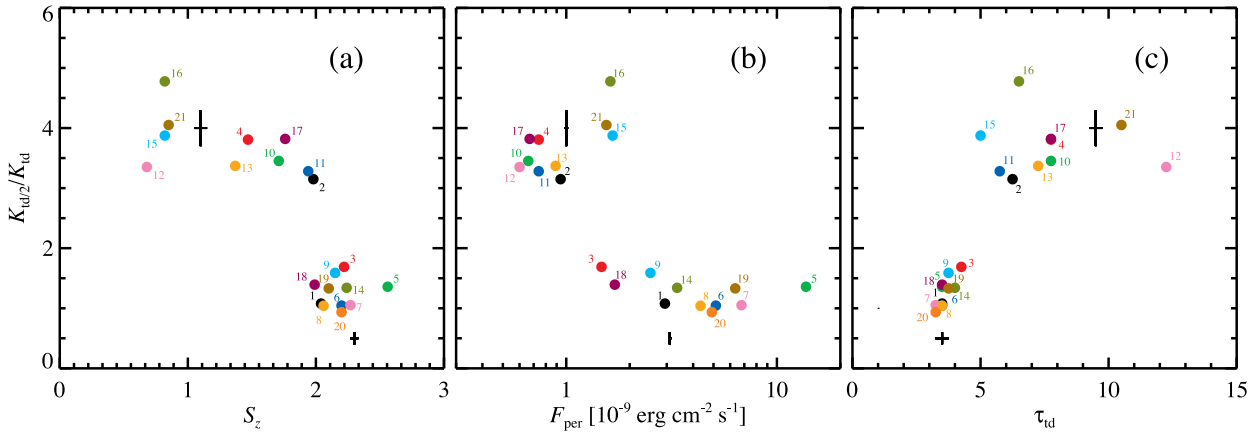

Figure 4. The K-ratio (i.e. the ratio of the blackbody normalization at 1/2 of the touchdown flux $K_{\rm td/2}$ to that at the touchdown $K_{\rm td}$) as a function of the (a) S_z value, (b) persistent flux $F_{\rm per}$ (in 2.5–25 keV band) before the burst, and (c) time between the burst start and the touchdown $\tau_{\rm td}$. Typical error bars are shown by black crosses. Bursts are numbered according to the order in Table 1 and identified by the same colours as in Fig. 3.

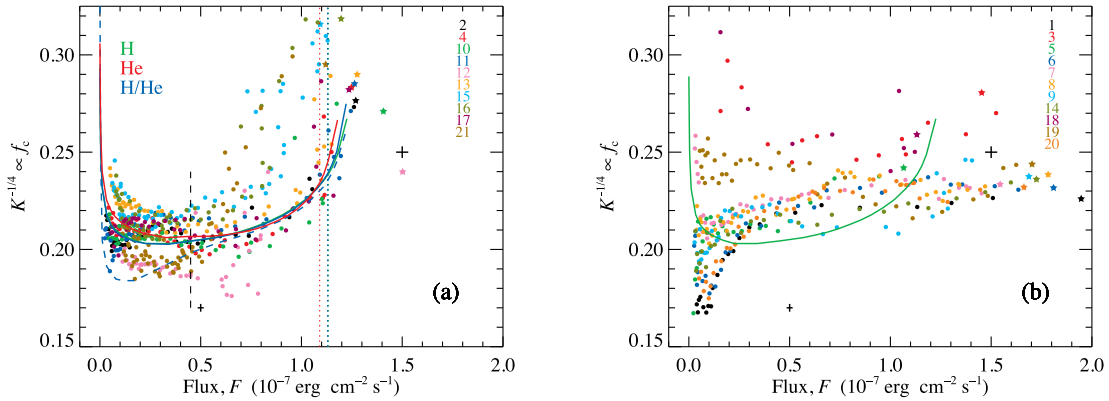

Figure 5. Evolution of $K^{-1/4}$ with flux during the cooling tail of the (a) hard-state (low accretion rate) and (b) soft-state (high accretion rate) bursts. The cooling tracks for different bursts are shown from the touchdown (marked by stars) to the end of the burst. The best-fitting theoretical models $Af_c(F/F_{\rm Edd})$ for $\log g = 14$ (Suleimanov, Poutanen & Werner 2012) to the combined data from the hard-state bursts 2, 4, 10, 11, 13 and 17 are shown by solid curves (pure helium – red, pure hydrogen – green, and solar mixture of H and He with sub-solar metal abundances of $Z = 0.01\,Z_\odot$ – blue, which nearly coincides with the green curve). The vertical dotted lines indicate the position of the Eddington flux $F = F_{\rm Edd}$. The dashed line marks the position of the minimum flux $F_{\rm min} = F_{\rm td}/e$ used in most of the fits. The black crosses indicate the typical error bars. The model for solar composition ($Z = Z_\odot$) shown by the dashed blue curve does not describe well the data at fluxes below half of the touchdown flux. For the soft-state bursts, the models do not fit the data well and only the hydrogen model from panel (a) is shown to guide the eye.

parameters (see Table 1) derived from the bursts (Figs 4b and c), such as the persistent flux prior to the bursts and the duration of the phase prior to the touchdown.

The bursts can be now separated into two distinct groups. The first group (bursts 2, 4, 10–13, 15–17 and 21) occur at $S_z \lesssim 2$ at low persistent fluxes and have $K_{\rm td/2}/K_{\rm td} > 2$ consistent with those predicted by the atmosphere models. The second group of bursts (1, 3, 5–9, 14, 18–20) happening at $S_z \gtrsim 2$, at higher persistent fluxes, on the other hand, has $K_{\rm td/2}/K_{\rm td} < 2$, inconsistent with theoretical predictions. Thus, the bursts can be cleanly separated into groups either by their K-ratio, or based on the shape of the spectrum of the persistent emission prior to the burst (Fig. 3), using, e.g., the source position on the colour–colour diagram (see Fig. 2), or duration of the super-Eddington phase $\tau_{\rm td}$ or the persistent flux (see Fig. 4).

The bursts from the first group occur at low accretion rate (with $F_{\rm per} \lesssim 0.015F_{\rm Edd}$), when the object is in the hard state. Here the persistent spectra are closer to a power law, produced most probably either in the hot inner flow of the accretion disc or the optically thin boundary layer (Kluzniak & Wilson 1991; Popham & Sunyaev 2001). In this situation, the evolution of $K^{-1/4}$ with flux during the bursts follows the theoretical models with very little metals (Suleimanov et al. 2011a, 2012) down to rather low luminosities (see Fig. 5a). The exception are two bursts: 12 and 21 [see pink and brown points in Fig. 5(a)]. Both show clear drop in $K^{-1/4}$ value at fluxes 0.3–0.5 of the touchdown flux. Interestingly, both bursts demonstrate two times longer (∼10 s versus ∼5 s) super-Eddington phase until the touchdown (see Table 1). We can speculate that in these bursts a lot of accreted material was blown away during this phase exposing the material rich in heavy elements (see Weinberg, Bildsten & Schatz 2006), resulting in strong edges in the observed X-ray band and reduction of the colour-correction factor (Suleimanov et al. 2011a, 2012).

The bursts from the second group occur at high persistent fluxes (with $F_{\rm per} \gtrsim 0.015F_{\rm Edd}$), when the source was in the soft state with the spectrum dominated by the blackbody-like radiation in the soft X-rays, probably coming from the boundary layer and the accretion disc (Gilfanov, Revnivtsev & Molkov 2003; Revnivtsev & Gilfanov 2006; Suleimanov & Poutanen 2006; Revnivtsev, Suleimanov & Poutanen 2013). These bursts have almost constant normalization K over a substantial range of luminosities, with a deviation seen only at fluxes below 20 per cent of the touchdown flux (see Fig. 5b). This evolution is not consistent with NS atmosphere models and therefore these bursts cannot be used for further interpretation with the aim to measure NS parameters. It is clear that some of the assumptions that the models are based on are not valid for those bursts. The most obvious explanation is that at higher accretion rates in the soft state the accreting matter influences the atmosphere by forcing the upper layer to rotate (Inogamov & Sunyaev 1999; Suleimanov & Poutanen 2006) and probably by heating them. This then affects the emerging spectrum so that the assumption of the passively cooling atmosphere is not valid anymore. Thus, it is clear that only the hard-state bursts, which show the predicted evolution, should be used to constrain NS mass and radius.

3.2 NS mass and radius in 4U 1608−52 from the hard-state bursts

First, we consider the constraints that can be obtained from individual bursts. Bursts 12 and 21 showing significantly different evolution were not included in further studies. We use the cooling tail method (see Appendix A and Suleimanov et al. 2011b) that requires that the evolution of the blackbody normalization with flux F after the touchdown (when the atmosphere radius is assumed to coincide with the NS radius) is to be described by the theoretical models of the evolution of the colour-correction factor. The dependence of $K^{-1/4}$ on the observed flux F is fitted by theoretical curves $Af_c(F/F_{\rm Edd})$ obtained from the most recent hot NS atmosphere models that account for Klein–Nishina reduction of the electron scattering opacity (Suleimanov et al. 2012) for three chemical compositions.

Because the data have errors in both directions, there are outliers and the distribution of points around the best-fitting curve does not follow a Gaussian, and the χ^2-statistics is not appropriate. Instead, we use a robust maximum likelihood estimator (Press et al. 2007) and minimize the merit function

$$L = \sum_i \ln\left(1 + \frac{z_i^2}{2}\right). \quad (1)$$

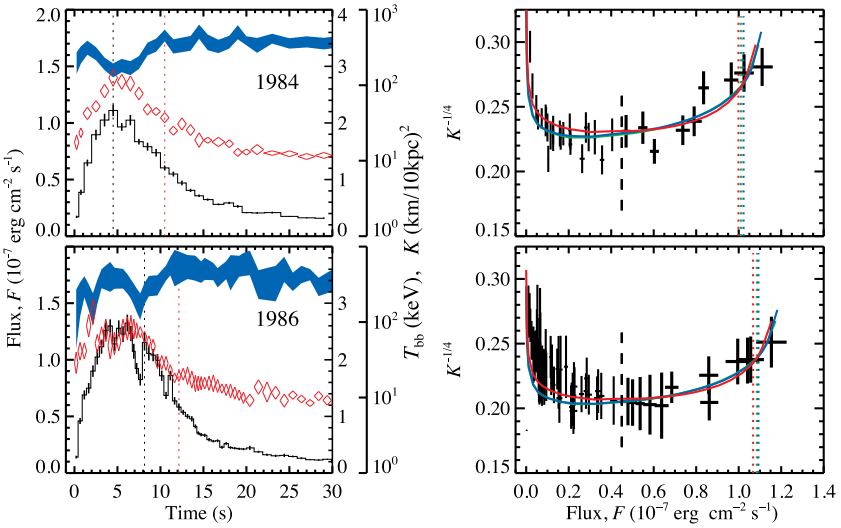

Figure 6. Left: time evolution of flux, temperature and blackbody normalization of the hard-state X-ray bursts observed by *EXOSAT* in 1984 and 1986 (Gottwald et al. 1987; Penninx et al. 1989). Right: same as Fig. 5, but for the *EXOSAT* bursts.

This introduces a Lorentzian weighting function into our maximum likelihood estimator that then removes the contribution from the most deviant outlier points but acts naturally with points that are close by. Here z_i is the normalized minimum distance of the ith data point from the model curve $\hat{y}(\hat{x})$:

$$z_i^2 = \frac{\left(\frac{x_i - \hat{x}}{\bar{\sigma}_x}\right)^2 + \left(\frac{y_i - \hat{y}}{\bar{\sigma}_y}\right)^2}{\left(\frac{\sigma_{x_i}}{\bar{\sigma}_x}\right)^2 + \left(\frac{\sigma_{y_i}}{\bar{\sigma}_y}\right)^2}, \quad (2)$$

where (x_i, y_i) are the coordinates for the ith data point (substitute F for x and $K^{-1/4}$ for y), $(\sigma_{x_i}, \sigma_{y_i})$ are the errors, and $\bar{\sigma}_x$ and $\bar{\sigma}_y$ are the mean errors in the x- and y-directions over all data points. The uncertainties in the best-fitting parameters are obtained with the bootstrap method.

The free parameters for the fits are the Eddington flux $F_{\rm Edd}$ and the quantity $A = (R_\infty[\mathrm{km}]/D_{10})^{-1/2}$, which is related to the observed NS radius at the infinity $R_\infty = R(1 + z)$ (here R is the circumferential NS radius and z is the surface redshift). We choose the atmosphere models with $\log g = 14.0$, because the results are rather insensitive to its choice (see below). Compositions considered are pure hydrogen (H), pure helium (He) and solar composition of H and He with sub-solar metal abundance of $Z = 0.01\,\mathrm{Z}_\odot$ (H/He). It seems that $Z < 0.1\,\mathrm{Z}_\odot$ in the surface layers, because in the opposite case the atmosphere model predicts a drop in $f_{\rm c}$ (and correspondingly in $K^{-1/4}$) at $F \sim 0.3F_{\rm Edd}$ (Suleimanov et al. 2011a, 2012), which is not observed. The low metal abundance might be caused by chemical stratification. For example, in mostly hydrogen atmosphere with the surface gravity $\log g = 14$ at $T \sim 10^7$ K and density at the photosphere of $\rho \approx 0.2\,\mathrm{g\,cm^{-3}}$, the iron settling time-scale is 3×10^{-4} s (see equation 9 in Brown, Bildsten & Chang 2002). This is smaller than the time required to accrete the photospheric layer of $\Sigma = 1\,\mathrm{g\,cm^{-2}}$ with accretion rate $\dot{M} \approx 10^{16}\,\mathrm{g\,s^{-1}}$ (corresponding to $F_{\rm per} = 10^{-9}\,\mathrm{erg\,cm^{-2}\,s^{-1}}$ and the distance of 5 kpc), $t_{\rm acc} = \Sigma\, 4\pi R^2/\dot{M} \approx 10^{-3}$ s. Alternatively, the absence of that drop can result from the temperature inversion because of accretion.

We also consider two bursts observed by *EXOSAT* during a very low hard state (Gottwald et al. 1987; Penninx et al. 1989), in spite of the fact that they do not seem to be PRE. We note that the cooling tail method allows us to determine the Eddington flux even for bursts not reaching the Eddington limit, because of the curvature in the $K^{-1/4}$ versus F dependence. For the two *EXOSAT* bursts, these dependences are well described by theoretical atmosphere models and are similar to the PRE hard-state bursts observed by *RXTE* (see Fig. 6).

The best-fitting values for A and $F_{\rm Edd}$ for the hard-state bursts (using the data from touchdown to $F_{\rm min} = F_{\rm td}/e$) are presented in Table 2. Note that the values of $F_{\rm Edd}$ are typically smaller by 10–15 per cent than the touchdown flux, mostly because of the difference between the actual electron scattering opacity and the Thomson one for which the Eddington flux is defined (Suleimanov et al. 2012). We also present in Table 2 the values of the Eddington temperature $T_{\rm Edd,\,\infty}$. This is an observable that allows us to get a distance-independent constraint on the NS mass–radius relation (see Appendix A). We see that most of the bursts give very similar results, except bursts 15, 16 and the *EXOSAT* burst from 1984 (Exo1), which show significantly smaller $F_{\rm Edd}$ and a larger A (i.e. much smaller blackbody normalization K), which could be a result of a confined burning. Burst 15 and Exo1 also might not be genuine PRE bursts as the temperature profile does not show a clear two-peak structure seen in other bursts. For illustration, we present in Fig. 7 the mass–radius constraints obtained from the measured values of $T_{\rm Edd,\,\infty}$ not accounting for errors and constraints on the distance assuming hydrogen atmosphere. We see that all bursts (except bursts 15 and Exo1 showing lower emitting area) give minimum NS radius of 13 km at $1.0 < M < 2.4\,\mathrm{M}_\odot$. For other atmosphere compositions, the radii are even larger. We note that pure He composition can be safely rejected, because it predicts a mass much below the mass-shedding limit for a star rotating at 620 Hz (Muno et al. 2002; Galloway et al. 2008). Solar H/He ratio is barely consistent with this constraint. The fact that only hydrogen-rich models give solutions above the mass-shedding limit is consistent with the orbital period of the system (∼0.5 d; see Wachter et al. 2002) and inferred companion.

We have selected *RXTE* bursts 2, 4, 10, 11, 13 and 17 that show consistent results and larger emitting area (increasing the chance that burning is happening over the whole NS surface, which is also

Table 2. Parameters of the fits of the $K^{-1/4}$–F dependence with the NS atmosphere models for various chemical compositions and $\log g = 14.0$.

No.	Composition	$F_{\rm Edd}$ (10^{-7} erg cm^{-2} s^{-1})	A ((km/10 kpc)$^{-1/2}$)	$T_{\rm Edd,\infty}$ (10^7 K)
		Individual bursts		
2	H	1.16 ± 0.05	0.137 ± 0.003	1.62 ± 0.03
	H/He	1.17 ± 0.03	0.138 ± 0.003	1.64 ± 0.03
	He	1.05 ± 0.05	0.143 ± 0.002	1.65 ± 0.03
4	H	1.10 ± 0.03	0.133 ± 0.002	1.55 ± 0.03
	H/He	1.10 ± 0.04	0.134 ± 0.003	1.57 ± 0.03
	He	1.08 ± 0.04	0.140 ± 0.003	1.62 ± 0.03
10	H	1.15 ± 0.03	0.132 ± 0.003	1.56 ± 0.03
	H/He	1.14 ± 0.03	0.133 ± 0.003	1.57 ± 0.03
	He	1.11 ± 0.03	0.139 ± 0.003	1.63 ± 0.03
11	H	1.17 ± 0.04	0.140 ± 0.003	1.65 ± 0.03
	H/He	1.17 ± 0.04	0.141 ± 0.003	1.67 ± 0.03
	He	1.16 ± 0.04	0.148 ± 0.003	1.75 ± 0.03
13	H	1.08 ± 0.04	0.140 ± 0.003	1.62 ± 0.03
	H/He	1.09 ± 0.04	0.141 ± 0.003	1.64 ± 0.04
	He	1.07 ± 0.04	0.148 ± 0.003	1.71 ± 0.03
15	H	0.99 ± 0.04	0.149 ± 0.003	1.69 ± 0.04
	H/He	1.00 ± 0.04	0.150 ± 0.003	1.71 ± 0.04
	He	0.97 ± 0.04	0.156 ± 0.003	1.76 ± 0.04
16	H	0.85 ± 0.03	0.143 ± 0.003	1.56 ± 0.04
	H/He	0.84 ± 0.03	0.144 ± 0.003	1.57 ± 0.04
	He	0.83 ± 0.03	0.151 ± 0.004	1.64 ± 0.04
17	H	1.14 ± 0.04	0.138 ± 0.003	1.62 ± 0.04
	H/He	1.13 ± 0.05	0.139 ± 0.003	1.63 ± 0.04
	He	1.06 ± 0.03	0.144 ± 0.004	1.66 ± 0.04
Exo1[a]	H	1.01 ± 0.05	0.153 ± 0.006	1.74 ± 0.07
	H/He	1.02 ± 0.05	0.155 ± 0.006	1.77 ± 0.07
	He	1.00 ± 0.06	0.161 ± 0.005	1.84 ± 0.06
Exo2[b]	H	1.09 ± 0.05	0.137 ± 0.006	1.60 ± 0.07
	H/He	1.09 ± 0.06	0.139 ± 0.006	1.62 ± 0.07
	He	1.07 ± 0.05	0.145 ± 0.006	1.67 ± 0.07
		Combined bursts 2, 4, 10, 11, 13 and 17		
All[c]	H	1.13 ± 0.05	0.137 ± 0.003	1.61 ± 0.04
	H/He	1.13 ± 0.05	0.138 ± 0.003	1.62 ± 0.04
	He	1.09 ± 0.06	0.144 ± 0.002	1.68 ± 0.03
All[d]	H	1.13 ± 0.06	0.137 ± 0.004	1.61 ± 0.05
	H/He	1.11 ± 0.06	0.138 ± 0.003	1.61 ± 0.04
	He	1.11 ± 0.05	0.145 ± 0.003	1.70 ± 0.04
All[e]	H	1.17 ± 0.05	0.140 ± 0.001	1.66 ± 0.02
	H/He	1.17 ± 0.04	0.141 ± 0.001	1.68 ± 0.02
	He	1.11 ± 0.05	0.145 ± 0.001	1.69 ± 0.02

Note. Errors correspond to the 90 per cent confidence level.
[a]Burst observed by *EXOSAT* in 1984.
[b]Burst observed by *EXOSAT* in 1986.
[c]Best-fitting parameters for the combined data for bursts 2, 4, 10, 11, 13 and 17 with the lower limit on the flux $F_{\rm min} = F_{\rm td}/e$.
[d]Same as case [c], but for $F_{\rm min} = 0.5F_{\rm td}$.
[e]Same as case [c], but for $F_{\rm min} = 0.1F_{\rm td}$.

visible) to construct a combined cooling track.[2] As in the case of individual bursts, we use the data down to $F_{\rm min} = F_{\rm td}/e$. The best-fitting atmosphere models for all considered chemical compositions are shown by solid curves in Fig. 5(a) and the parameters are presented in Table 2. The parameters lie very close to the mean values obtained from individual bursts. The errors are similar to those for individual bursts, because of a rather large spread of their cooling curves. The blackbody normalization in the cooling tail is $K \approx 570$ (km/10 kpc)^2. Interestingly, the best-fitting parameters for pure H and solar H/He ratio (with $Z = 0.01\,{\rm Z}_\odot$) composition models are nearly identical. We have also checked how the data selection affects the best-fitting parameters. For the lower flux limit of $F_{\rm min} = 0.5F_{\rm td}$, the parameters hardly change at all. However, taking $F_{\rm min} = 0.1F_{\rm td}$ results in values for $F_{\rm Edd}$, A and $T_{\rm Edd,\infty}$ higher by 2–3 per cent for H and solar models. For He model, results are nearly independent of the data selection, because it describes the data somewhat better in a wider flux interval.

[2] We note here that the hard-state bursts excluded from this analysis are 12, 15, 16 and 21, all occurring at a low state at $S_z < 1$.

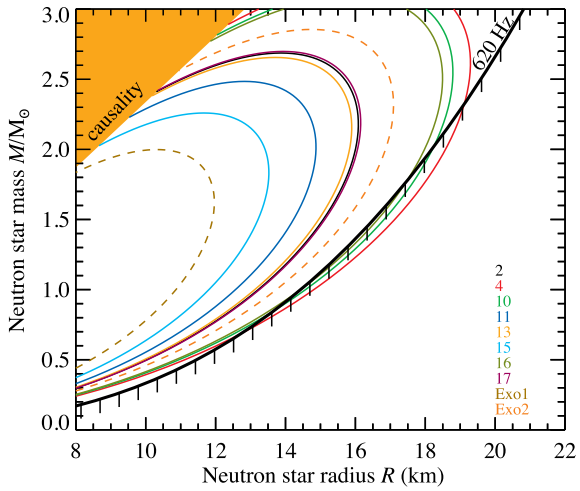

Figure 7. Mass–radius constraints coming from individual hard-state bursts of 4U 1608−52 based only on the measured value of $T_{\rm Edd,\infty}$ assuming hydrogen atmosphere. The upper-left region is excluded by constraints from the causality requirements (Haensel et al. 2007; Lattimer & Prakash 2007). The constraints for the *EXOSAT* bursts are shown by the dashed curves. The lower-right region marked by black curve with downward ticks lies below the mass-shedding limit (Lattimer & Prakash 2007) for the observed rotational frequency of 620 Hz.

We further use the best-fitting A and $F_{\rm Edd}$ for the set of combined bursts (and $F_{\rm min} = F_{\rm td}/e$) to constrain the NS mass and radius. Pure helium models can be rejected just from the value of $T_{\rm Edd,\infty}$ [see Table 2 and the solid red curve in Fig. 8(a)], because they either give a mass lying below the mass-shedding limit or extremely high masses of $>4\,{\rm M}_\odot$. The solar composition models predict M–R dependence obtained from $T_{\rm Edd,\infty}$ that nearly coincides with the mass-shedding limit [see solid blue curve in Fig. 8(a)], restricting the hydrogen mass fraction to $X \gtrsim 0.7$. Because of the nature of the companion star (Wachter et al. 2002), there is no reason to take the hydrogen fraction below the solar value; therefore, we assume a uniform distribution of X in the interval from 0.74 to 1. For the values of $F_{\rm Edd}$ and A for different X, we use linear interpolation between the corresponding values for $X = 0.74$ and 1. We further assume a probability distribution function for the distance D to 4U 1608−52 to follow a Gaussian with the mean and standard deviation of 5.8 and 2.0 kpc, respectively (see Section 2.1). Using Monte Carlo simulations, we simulate D and X and convert a distribution of A and $F_{\rm Edd}$ (obtained with a bootstrap) to the distribution of M and R (see Suleimanov et al. 2011b and Appendix A). We reject the solutions below the mass-shedding limit and with $M < 1.0\,{\rm M}_\odot$ to be consistent with the NS formation scenarios (Woosley, Heger & Weaver 2002) and the minimum observed pulsar masses (Kiziltan et al. 2013). We also reject solutions with $M > 3\,{\rm M}_\odot$, because there are no modern EoS that support such massive NS. The resulting banana-like contours (see Fig. 8a) are very much elongated along the curves of constant Eddington temperature $T_{\rm Edd,\infty}$, which is just a result of a large uncertainty in distance. The width of the banana is defined by the errors in $T_{\rm Edd,\infty}$ and by the width of the distribution of X. The NS radius is constrained above 13 km (at 90 per cent confidence) independently of the metal abundance for NS masses in the range 1.0–2.4 $\,{\rm M}_\odot$. Note, however, that the radius becomes about 1 km smaller if we use $F_{\rm min} = 0.1 F_{\rm td}$ [see red dashed contours in Fig. 8(a)]. Thus, the conservative lower limit for R is 12 km. Our results are consistent with the stiff EoS of cold dense matter that also has support from the recent observations of NS with $M \approx 2\,{\rm M}_\odot$ (Demorest et al. 2010; Antoniadis et al. 2013).

We see that one branch of the solutions (high mass–small radius) corresponds to a larger gravity than was assumed in the fits ($\log g = 14.0$). Taking an atmosphere model for $\log g = 14.6$ does not affect at all the solutions for $F_{\rm min} = F_{\rm td}/e$, but for $F_{\rm min} = 0.1\,F_{\rm td}$ (red contours) it shifts the contours (upper-left branch) down by $0.2\,{\rm M}_\odot$.

We note that for the best-fitting $F_{\rm Edd,-7} = 1.13$ and $A = 0.137$–0.138, the solution for M and R exists only for D_{10} below the upper limits $D_{10,\rm max} = 0.45$ and 0.50 for H ($X = 1$) and solar

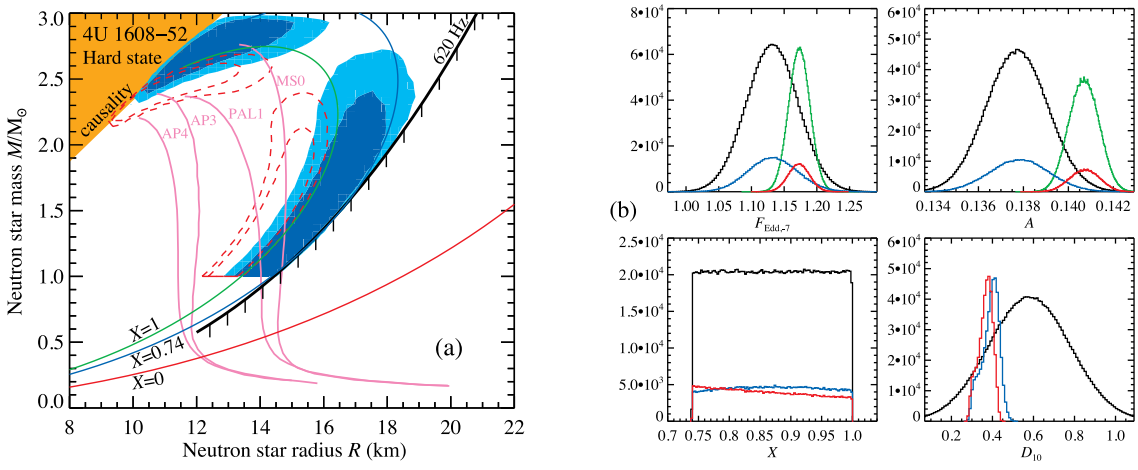

Figure 8. (a) Mass–radius constraints from the hard-state bursts of 4U 1608−52 for a distance of 5.8 ± 2.0 kpc assuming $1.0 < M/{\rm M}_\odot < 3.0$ and $0.74 < X < 1$. The dark and light blue contours correspond to 90 and 68 per cent confidence limits for $F_{\rm min} = F_{\rm td}/e$. For $X \lesssim 0.7$, solutions lie below the mass-shedding limit for a rotational frequency of 620 Hz marked by the black curve with downward ticks. The dashed red contours are similar constraints for $F_{\rm min} = 0.1\,F_{\rm td}$. Solid green, blue and red curves correspond to the best-fitting $T_{\rm Edd,\infty}$ for the combined bursts (with $F_{\rm min} = F_{\rm td}/e$), assuming H, solar H/He ratio and He composition, respectively. The NS mass–radius relations for several EoS of cold dense matter that do not contradict the existence of $2\,{\rm M}_\odot$ pulsars (Demorest et al. 2010; Antoniadis et al. 2013) are shown by pink curves. (b) Corresponding distributions of parameters from the analysis of the hard-state bursts. The black and green histograms are the prior parameter distributions, and the blue and red histograms are the posterior distributions of parameters that give a physical solution (see Appendix A) for $F_{\rm min} = F_{\rm td}/e$ and $F_{\rm min} = 0.1\,F_{\rm td}$, respectively. For some parameters, there are two solutions; therefore, the posterior distributions can exceed the prior one.

ratio H/He ($X = 0.74$) atmosphere, respectively (see equation A13). At the maximum possible distance, the solution has to lie at the turning point (furthest from the origin of coordinates) of the curve of constant $T_{\rm Edd,\,\infty}$ on the M–R plane. For a given distance $D < D_{\rm max}$, there are two solutions for M and R corresponding to u_- (lower) and u_+ (upper) branches of solutions (A12). They can be found by substituting into equations (A9) the solutions obtained via equations (A11) and (A12) using the observables A and $F_{\rm Edd}$ as well as the distance D. Restriction on the NS mass $M > 1.2\,{\rm M}_\odot$ thus puts the lower limit on the distance $D_{10} > D_{10,\,\rm min} = 0.3$ and 0.32 for $X = 1$ and 0.74, respectively. The presented error contours are barely consistent with the existing theoretical M–R relations and at higher masses they are deviating even more (see Fig. 8a). Thus, it is likely that the NS mass in 4U 1608−52 is not much larger than the typically measured 1.4–1.5 $\rm M_\odot$. For $M \in [1.2,\,1.5]\,{\rm M}_\odot$, the distance has to lie in a rather narrow range between 3.1 and 3.7 kpc.

If instead we follow the assumption of Güver et al. (2010a) and introduce a sharp cut in the distance distribution at $D_{\rm min} = 3.9$ kpc, the size of the contours in Fig. 8 will be significantly reduced. For example, for $X = 1$ the contours will close at $M > 1.9\,{\rm M}_\odot$, which results in $R > 15$ km (for $M < 2.4\,{\rm M}_\odot$), while for $X = 0.74$ similar constraints are $M > 1.6\,{\rm M}_\odot$ and $R > 16$ km. It is clear that such a cut in D would not produce realistic results for these bursts.

We note here that all the constraints obtained here are based on NS atmosphere model for non-rotating stars. Because 4U 1608−52 rotates 620 times a second, the shape of the NS is distorted and the emission cannot possibly be spherically symmetric. Rapid rotation also boosts radiation emitted along the equatorial plane and hardens the spectrum. Including effects of rapid rotation would reduce the radius of the non-rotating NS determined from the cooling tail method by about 10 per cent depending on the inclination (Suleimanov et al., in preparation).

3.3 Comparison to the soft-state bursts and the touchdown method

Let us now take a look at the soft-state bursts. Because the evolution of $K^{-1/4}$ with flux does not follow the predicted theoretical dependence, this theory cannot be used to get $f_{\rm c}$ and, therefore, it is meaningless to use these data to determine NS parameters (using the cooling tail or any other method). However, to demonstrate the main difference in the NS mass–radius constraints from the hard- and the soft-state bursts, we apple the touchdown method as was done for 4U 1608−52 by Güver et al. (2010a).

First, for the touchdown method, we need to find the blackbody normalization in the cooling tail. Looking at Fig. 5(b), we see that the typical value of $K^{-1/4}$ is about 0.23, which translates to $K \approx 350$. Secondly, the flux at touchdown (which is *assumed* to be equal to the Eddington flux $F_{\rm Edd}$) for most bursts is between 1.0 and 2.0, with the average of about 1.6×10^{-7} erg cm^{-2} s^{-1} [see stars in Fig. 5(b) and Table 1]. These values are similar to those determined by Güver et al. (2010a): $F_{\rm Edd} = (1.541 \pm 0.065) \times 10^{-7}$ erg cm^{-2} s^{-1} and $K = 324.6 \pm 2.4$ in the cooling tail, which we adopt for easier comparison.[3] They correspond to $T_{\rm Edd,\,\infty} = 2.14 \times 10^7$ K and the maximum possible distance $D_{10,\,\rm max} = 0.405$ at $f_{\rm c} = 1.4$, $X = 0$ and central values for $F_{\rm Edd}$ and K (see equation A13). Taking $f_{\rm c}$ smaller and X larger decreases $D_{\rm max}$ further. We note here that in the hard-state bursts K is larger by a factor of 1.75, $F_{\rm Edd}$ is smaller by 50 per cent and $T_{\rm Edd,\,\infty}$ is smaller by ∼30 per cent.

We now can use these observables to obtain the NS mass and radius distribution. We follow here the assumptions by Güver et al. (2010a): we take a uniform distribution of $f_{\rm c}$ between 1.3 and 1.4 (although the actual value for He atmosphere is closer to 1.5; see Suleimanov et al. 2012), and assume a uniform distribution of the hydrogen fraction X between 0 and 0.7 (this is also questionable, because the companion star is likely hydrogen rich; see Wachter et al. 2002). However, for the distance D distribution, we take a Gaussian with the mean 5.8 kpc and 1σ of 2 kpc. These distributions are shown by black (or green for D and parameter α, see Appendix A) histograms in Fig. 9(b). The posterior distributions of parameters that give a physical solution for M and R are shown by blue histograms. The solution exists for about 10 per cent of all parameters (just because of the constraint $D < D_{\rm max} \approx 4$ kpc). The resulting NS mass and radius are very small [see blue contours in Fig. 9(a)] with the best-fitting R being below 8 km, because the peak in the distance distribution is at ∼2 kpc. If we take a distribution of X extending to 1, the solutions will be even more extended towards lower radii. On the other hand, extending $f_{\rm c}$ towards 1.5 leads to extension of the contours to radii up to 12 km and masses to $2\,{\rm M}_\odot$. Cutting the NS mass distribution say at $M > 1.2\,{\rm M}_\odot$ leaves two separated regions: $R \in [5,\,8]$ km for larger mass $M \in [1.2,\,1.6]\,{\rm M}_\odot$ and $R \in [7,\,9]$ km for $M \in [1.2,\,1.35]\,{\rm M}_\odot$.

These results are very different from $M = 1.74 \pm 0.14\,{\rm M}_\odot$ and $R = 9.3 \pm 1.0$ km obtained by Güver et al. (2010a) from the same data.[4] The only difference in our approach is that we did not cut the distance distribution. To illustrate this, we now apply such a cut, leaving only $D > 3.9$ kpc. The posterior distributions of parameters that give a physical solution are shown by red histograms in Fig. 9(b). Only a fraction of about 6×10^{-4} of parameters A, $F_{\rm Edd}$ and D from the assumed prior distributions produce a physical solution for the NS mass and radius [note that in Fig. 9(b) the posterior distributions are multiplied by a factor of 300]. We see that the posterior distribution of $F_{\rm Edd}$ is strongly skewed towards smaller flux by $\sim 1.5\sigma$, the $f_{\rm c}$ distribution is skewed towards larger values and the allowed chemical composition is nearly pure helium with $X < 0.1$ (which contradicts the nature of the companion; Wachter et al. 2002), and the distribution of parameter α (see equation A11) and the distance distribution are nearly a δ-function (because all solutions have to lie between the cutoff at 3.9 kpc and $D_{\rm max} = 4.05$ kpc). Thus, it is clear that the values for the best-fitting M and R and their small errors [see red contours in Fig. 9(a)] are fully determined by an unrealistic assumption of the sharp cutoff in the distance distribution and a cut in the distribution of $f_{\rm c}$ at 1.4.

The problem that a very small fraction of the parameter space gives a physical solution was noticed previously by Steiner et al. (2010). As a solution, they suggested to relax an assumption that the touchdown moment corresponds to the photosphere being at the NS surface. They, however, adopted all the observables given in Güver et al. (2010a) and assumed the same distance distribution with the unphysical cutoff. We showed here that parameters (K, $F_{\rm Edd}$, X or $f_{\rm c}$) presented by Güver et al. (2010a) are very different from those we obtain from the hard-state bursts, and the combination of these parameters with the cut in the distance distribution was responsible not only in small errors and the values of the determined M and R

[3] They have used bursts 1 and 8 from Table 1 for determination of the touchdown flux, and bursts 6, 7 and 8 and one non-PRE burst to measure the blackbody normalization of the cooling tail.

[4] The errors on the NS mass and radius obtained by Güver et al. (2010a) are extremely small, i.e. much smaller than the uncertainties in the distance; they just reflect the statistical errors on K and $F_{\rm Edd}$.

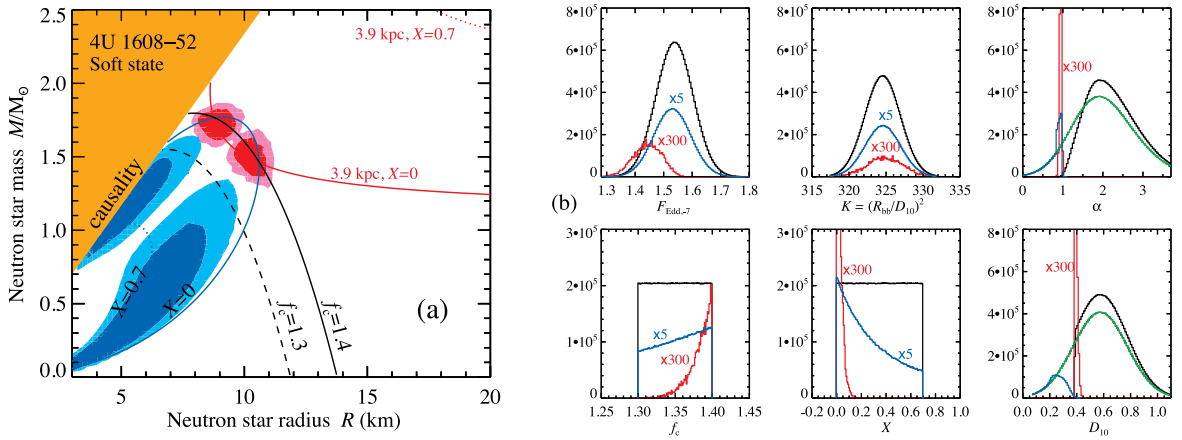

Figure 9. (a) Mass–radius constraints from the analysis of the soft-state bursts from 4U 1608−52–he lower-left dark and light blue contours (for 68 and 90 per cent confidence limits) represent the constraints under an assumption of the normal distribution of the distance, while the red and pink contours (for 68 and 90 per cent confidence limits) correspond to a similar analysis with the cut in the distance distribution at 3.9 kpc (Güver et al. 2010a). Both constraints are unreliable, because the soft-state bursts do not follow the theoretical models these results are based on. The red curves show the constraints from the value of $F_{\rm Edd}$ and the blue curves give constraints from the values of $T_{\rm Edd,\,\infty}$ assuming $f_{\rm c} = 1.4$. The solid curves correspond to pure He case, $X = 0$, and the dotted curves are for $X = 0.7$. The black curves give the constraint from K taking $f_{\rm c} = 1.4$ (solid) and $f_{\rm c} = 1.3$ (dashed) for $D = 3.9$ kpc. We see that only when simultaneously $X \approx 0$, $f_{\rm c} \gtrsim 1.4$ and $D \lesssim 4$ kpc, the curve do cross and a solution exists. (b) Corresponding distributions of the parameters. The Monte Carlo simulations were run with 2×10^7 points. The black histograms are the prior parameter distributions used by Güver et al. (2010a), with the distance distribution having a cutoff at 3.9 kpc. The green histograms give the distributions of D and α without such a cutoff. The red histograms (multiplied by 300) are the posterior distributions of parameters that give a physical solution (see Appendix A) for the first case, while the blue histograms are similar distributions for the normal distance distribution.

but also in the smallness of the parameter space giving solutions. Thus, the solution to the problem actually lies in picking up different bursts that do follow the theoretical atmosphere models.

Similar problems appear in the analysis of a number of other sources, e.g., 4U 1820−30 (Özel et al. 2009) and EXO 1745−248 (Güver et al. 2010b). All these bursts, which were used to determine the NS mass and radius, happened at high accretion rate, and did not follow the spectral evolution predicted by the theoretical atmosphere models. The errors on mass and radius in these sources were also very small, again due to an artificial sharp cut in the distance distribution, which fully determined the outcome (see Suleimanov et al. 2011b for a discussion). In recent papers, on KS 1731−260 (Özel, Gould & Güver 2012) and SAX J1748.9−2021 (Güver & Özel 2013), the cuts in the distance distribution were not applied, and as a result, the *M*–*R* contours extended to the lower-left corner, similarly to our blue contour in Fig. 9(b), which then could be reduced by constraining the mass, e.g., at $M > 1.2\,{\rm M}_\odot$. For both sources, however, the analysed bursts again did not follow theoretical evolution and thus the results are dubious.

Because the cooling tracks for the soft-state bursts do not follow theoretically predicted behaviour for a passively cooling NS, it is not surprising that the results for the NS mass and radius determination are very much different for the soft- and the hard-state bursts. There are also physical reasons that explain the difference. First, at high accretion rate, the accretion disc blocks half of the NS. Secondly, the colour-correction factor in the soft-state bursts is expected to be much larger than the usually assumed ∼1.4, if a significant part of the burst radiation has to pass through the rapidly rotating spreading layer above the NS surface (Inogamov & Sunyaev 1999), which has a reduced effective gravity due to the centrifugal support, leading to a flux through the atmosphere that is close to the local Eddington limit and has a high colour correction $f_{\rm c} \approx 1.6$–1.8 (Suleimanov & Poutanen 2006). These effects together naturally explain why the blackbody normalization is constant and much smaller during the cooling tail of the soft bursts (Suleimanov et al. 2011b). It is clear that the constancy of the blackbody area alone cannot be used as an argument in favour of visibility of the whole star. Moreover, the constancy of the apparent area contradicts theoretical atmosphere models. The presence of the accretion disc also reflects a part of the burst radiation breaking the spherical symmetry, increasing the observed flux at some angles (Lapidus & Sunyaev 1985) and leading to a higher touchdown flux in the soft-state bursts. This effect has been observed in superbursts (Ballantyne & Strohmayer 2004; Keek et al. 2014).

We conclude that as the variations in $K^{-1/4}$ as a function of flux do not follow theoretical predictions, these bursts cannot presently be used reliably to infer NS *M* and *R*.

4 SUMMARY

We studied 21 PRE bursts from 4U 1608−52 and found a clear dependence of the spectral evolution in the cooling tail of the bursts on the spectral state of the persistent emission prior to the burst. The same dependence can be also seen from various other model-independent parameters. We showed that the bursts observed during the hard state at low accretion rates are consistent with theoretical predictions of the NS atmosphere models, while the spectral evolution of the soft-state bursts is inconsistent with the theory. Such a behaviour is ubiquitous in the atoll sources (see Kajava et al. 2014). This implies that the basic assumption of the passively cooling NS atmosphere breaks down in these bursts. We argue that only the hard-state bursts at persistent luminosities below a few per cent of Eddington with the colours of the persistent emission characterized by $1 < S_z < 2$ can be used in efforts of determination of the NS masses and radii from the thermal emission of X-ray bursts.

We applied the most recent set of NS atmosphere models that account for Klein–Nishina reduction of electron opacity to the data of the hard-state PRE bursts of 4U 1608−52 and obtained the Eddington flux and the apparent angular size of the NS. From these

values, we constrain the mass and radius of the NS. Because of a large uncertainty in the distance, the solution lies along a long strip of constant Eddington temperature. For typically assumed and measured NS masses between 1.0 and 2.4 $M_\odot$, the NS radius is strongly constrained to be above 12 km. For the most probable range of masses 1.2–1.6 $M_\odot$, R is restricted to be between 13 and 16 km. These constraints are similar to that found for 4U 1724−307 (Suleimanov et al. 2011b) and support a stiff EoS for the cold, dense matter of the NS interior. These are also consistent with the recent discoveries of the 2 $M_\odot$ pulsars (Demorest et al. 2010; Antoniadis et al. 2013). We note, however, that the NS parameters are obtained assuming spherically symmetric non-rotating NS, covered by an atmosphere with homogeneous distributions of the effective temperature, surface gravity and chemical composition, and described by a single plane-parallel model atmosphere. Rapid rotation, however, breaks the symmetry and affects the NS shape, the observed flux and the colour temperature. A preliminary study (Suleimanov et al., in preparation) indicates that for an NS in 4U 1608−52 which rotates at 620 Hz, the lower limit on the radius of the non-rotating NS may be reduced by as much as 10 per cent. In this case, constraints on the NS radius from X-ray bursts become consistent with those coming from nuclear physics (Lattimer & Steiner 2014a).

Finally, we note that constraints on the NS masses and radii obtained from the soft-state and/or high accretion rate bursts that do not follow theoretically predicted spectral evolution (Özel et al. 2009, 2012; Güver et al. 2010a,b; Steiner et al. 2010; Güver & Özel 2013; Lattimer & Steiner 2014a) have to be revisited.

ACKNOWLEDGEMENTS

The research was supported by Academy of Finland grant 268740 (JP), the Väisälä Foundation (JN and JJEK), the Jenny and Antti Wihuri Foundation and the Magnus Ehrnrooth Foundation (JP and VS), the Finnish Doctoral Programme in Astronomy and Space Physics and the Emil Aaltonen Foundation (JJEK). VS acknowledges funding from the German Research Foundation (DFG) grant SFB/Transregio 7 'Gravitational Wave Astronomy' and the Russian Foundation for Basic Research (grant 12-02-97006-r-povolzhe-a). DKG acknowledges the support of an Australian Research Council Future Fellowship (project FT0991598). We acknowledge the support of the COST Action MP1104 and of the International Space Science Institute (Bern, Switzerland), where part of this investigation was carried out. This research has made use of data provided by the High Energy Astrophysics Science Archive Research Center (HEASARC), which is a service of the Astrophysics Science Division at NASA/GSFC and the High Energy Astrophysics Division of the Smithsonian Astrophysical Observatory.

REFERENCES

Antoniadis J. et al., 2013, Science, 340, 448
Arnaud K. A., 1996, in Jacoby G. H., Barnes J., eds, ASP Conf. Ser. Vol. 101, Astronomical Data Analysis Software and Systems V. Astron. Soc. Pac., San Francisco, p. 17
Ballantyne D. R., Strohmayer T. E., 2004, ApJ, 602, L105
Brown E. F., Bildsten L., Chang P., 2002, ApJ, 574, 920
Chamel N., Haensel P., Zdunik J. L., Fantina A. F., 2013, Int. J. Mod. Phys. E, 22, 30018
Churazov E., Gilfanov M., Forman W., Jones C., 1996, ApJ, 471, 673
Damen E., Magnier E., Lewin W. H. G., Tan J., Penninx W., van Paradijs J., 1990, A&A, 237, 103
Demorest P. B., Pennucci T., Ransom S. M., Roberts M. S. E., Hessels J. W. T., 2010, Nature, 467, 1081
Ebisuzaki T., 1987, PASJ, 39, 287
Galloway D. K., Muno M. P., Hartman J. M., Psaltis D., Chakrabarty D., 2008, ApJS, 179, 360
Gilfanov M., Revnivtsev M., Molkov S., 2003, A&A, 410, 217
Gottwald M., Stella L., White N. E., Barr P., 1987, MNRAS, 229, 395
Grindlay J. E. et al., 1980, ApJ, 240, L121
Guillot S., Servillat M., Webb N. A., Rutledge R. E., 2013, ApJ, 772, 7
Güver T., Özel F., 2013, ApJ, 765, L1
Güver T., Özel F., Cabrera-Lavers A., Wroblewski P., 2010a, ApJ, 712, 964
Güver T., Wroblewski P., Camarota L., Özel F., 2010b, ApJ, 719, 1807
Haensel P., Potekhin A. Y., Yakovlev D. G., 2007, Astrophysics and Space Science Library, Vol. 326, Neutron Stars 1: Equation of State and Structure. Springer, New York
Inogamov N. A., Sunyaev R. A., 1999, Astron. Lett., 25, 269
Jahoda K., Markwardt C. B., Radeva Y., Rots A. H., Stark M. J., Swank J. H., Strohmayer T. E., Zhang W., 2006, ApJS, 163, 401
Kajava J. J. E. et al., 2014, MNRAS, preprint (arXiv:1406.0322)
Kato S., Fukue J., Mineshige S., 1998, Black-Hole Accretion Disks. Kyoto Univ. Press, Kyoto
Keek L., in't Zand J. J. M., Kuulkers E., Cumming A., Brown E. F., Suzuki M., 2008, A&A, 479, 177
Keek L., Ballantyne D. R., Kuulkers E., Strohmayer T. E., 2014, ApJ, preprint (arXiv:1403.4940)
Kiziltan B., Kottas A., De Yoreo M., Thorsett S. E., 2013, ApJ, 778, 66
Kluzniak W., Wilson J. R., 1991, ApJ, 372, L87
Kramer M., Stairs I. H., 2008, ARA&A, 46, 541
Kuulkers E., Homan J., van der Klis M., Lewin W. H. G., Méndez M., 2002, A&A, 382, 947
Kuulkers E., den Hartog P. R., in't Zand J. J. M., Verbunt F. W. M., Harris W. E., Cocchi M., 2003, A&A, 399, 663
Lapidus I. I., Sunyaev R. A., 1985, MNRAS, 217, 291
Lattimer J. M., 2012, Annu. Rev. Nucl. Part. Sci., 62, 485
Lattimer J. M., Prakash M., 2007, Phys. Rep., 442, 109
Lattimer J. M., Schutz B. F., 2005, ApJ, 629, 979
Lattimer J. M., Steiner A. W., 2014a, Eur. Phys. J. A, 50, 40
Lattimer J. M., Steiner A. W., 2014b, ApJ, 784, 123
Lewin W. H. G., Vacca W. D., Basinska E. M., 1984, ApJ, 277, L57
Lewin W. H. G., van Paradijs J., Taam R. E., 1993, Space Sci. Rev., 62, 223
Lyne A. G. et al., 2004, Science, 303, 1153
Muno M. P., Chakrabarty D., Galloway D. K., Psaltis D., 2002, ApJ, 580, 1048
Nakamura N., Dotani T., Inoue H., Mitsuda K., Tanaka Y., Matsuoka M., 1989, PASJ, 41, 617
O'Connell R. F., 2004, Phys. Rev. Lett., 93, 081103
Penninx W., Damen E., van Paradijs J., Tan J., Lewin W. H. G., 1989, A&A, 208, 146
Popham R., Sunyaev R., 2001, ApJ, 547, 355
Press W. H., Teukolsky S. A., Vetterling W. T., Flannery B. P., 2007, Numerical Recipes: The Art of Scientific Computing. Cambridge Univ. Press, Cambridge
Revnivtsev M. G., Gilfanov M. R., 2006, A&A, 453, 253
Revnivtsev M. G., Suleimanov V. F., Poutanen J., 2013, MNRAS, 434, 2355
Steiner A. W., Lattimer J. M., Brown E. F., 2010, ApJ, 722, 33
Suleimanov V., Poutanen J., 2006, MNRAS, 369, 2036
Suleimanov V., Poutanen J., Werner K., 2011a, A&A, 527, A139
Suleimanov V., Poutanen J., Revnivtsev M., Werner K., 2011b, ApJ, 742, 122
Suleimanov V., Poutanen J., Werner K., 2012, A&A, 545, A120
Tawara Y., Hayakawa S., Kii T., 1984, PASJ, 36, 845
Titarchuk L., 1994, ApJ, 434, 570
van der Klis M., 1995, in Lewin W. H. G., van Paradijs J., van den Heuvel E. P. J., eds, Cambridge Astroph. Ser. No. 26. X-ray Binaries. Cambridge Univ. Press, Cambridge, p. 252
van Paradijs J., Dotani T., Tanaka Y., Tsuru T., 1990, PASJ, 42, 633
Wachter S., Hoard D. W., Bailyn C. D., Corbel S., Kaaret P., 2002, ApJ, 568, 901

Weinberg N. N., Bildsten L., Schatz H., 2006, ApJ, 639, 1018
Woosley S. E., Heger A., Weaver T. A., 2002, Rev. Mod. Phys., 74, 1015
Worpel H., Galloway D. K., Price D. J., 2013, ApJ, 772, 94
Özel F., Güver T., Psaltis D., 2009, ApJ, 693, 1775
Özel F., Gould A., Güver T., 2012, ApJ, 748, 5

APPENDIX A: THE COOLING TAIL METHOD

For completeness, we present the cooling tail method (Suleimanov et al. 2011a,b) that is used in the paper to constrain the NS mass and radius. In order to achieve this goal, we need measurements of the apparent area of the NS and the Eddington flux. Knowing the distance to the source is also a prerequisite for accurate calculations.

We define the Eddington flux as

$$F_{\rm Edd} = \frac{GMc}{D^2\kappa_{\rm e}(1+z)}, \tag{A1}$$

where $\kappa_{\rm e} = 0.2(1+X)$ cm^2 g^{-1} is the electron scattering opacity, X is the hydrogen mass fraction, D is the distance to the source,

$$1+z = (1-u)^{-1/2} = \left(1-2GM/Rc^2\right)^{-1/2} \tag{A2}$$

is the surface redshift, $u = R_{\rm S}/R$, R is the NS stellar circumferential radius, $R_{\rm S} = 2GM/c^2$ is the Schwarzschild radius and M is the NS gravitational mass. Such a definition of the Eddington flux explicitly assumes that the opacity is dominated by electron scattering and the cross-section is equal to the Thomson one. For the case of hot atmospheres of NS with the surface temperature of about 3–3.5 keV, which correspond to the Eddington flux at the NS surface for $\log g =$ 14–14.5, the Rosseland mean Compton scattering opacity is about 7–10 per cent lower that the Thomson one, resulting in an Eddington limit which is larger by the same amount (Suleimanov et al. 2012). This immediately implies that even if the Eddington limit is reached at the touchdown, the flux at this moment has to be larger than $F_{\rm Edd}$, which is defined for Thomson opacity.

At luminosities close to the Eddington, the spectrum of the NS is close to a diluted blackbody $F_E \approx wB_E(T_{\rm c} = f_{\rm c}T_{\rm eff})$, where $T_{\rm eff}$ and $T_{\rm c}$ are the effective and colour temperatures measured at the NS surface, $f_{\rm c}$ is the colour-correction factor and w is the dilution factor which is close to $1/f_{\rm c}^4$. The observed bolometric blackbody flux is

$$F = \sigma_{\rm SB}T_{\rm bb}^4\frac{R_{\rm bb}^2}{D^2} = \sigma_{\rm SB}T_{\infty}^4\frac{R_{\infty}^2}{D^2}, \tag{A3}$$

where $R_\infty = R(1+z)$ is the apparent NS radius, T_∞ is the redshifted effective temperature and $T_{\rm bb}$ is the measured colour temperature. The temperatures are related as

$$T_{\rm bb} = f_{\rm c}\,T_\infty = f_{\rm c}\,\frac{T_{\rm eff}}{1+z} = \frac{T_{\rm c}}{1+z}. \tag{A4}$$

We then get the relation between the blackbody normalization and the NS radius

$$\frac{R_{\rm bb}^2}{D^2} = \frac{R^2}{D^2}\frac{(1+z)^2}{f_{\rm c}^4} = \frac{R_\infty^2}{D^2}\frac{1}{f_{\rm c}^4}, \tag{A5}$$

which can be easily transformed to (Penninx et al. 1989; van Paradijs et al. 1990)

$$K^{-1/4} = f_{\rm c}A, \qquad A = (R_\infty[{\rm km}]/D_{10})^{-1/2}, \tag{A6}$$

where $K = (R_{\rm bb}[{\rm km}]/D_{10})^2$ and $D_{10} = D/10\,{\rm kpc}$. We can rewrite this as

$$R_\infty = R(1+z) = D_{10}A^{-2} = D_{10}\sqrt{K}\,f_{\rm c}^2\ {\rm km}. \tag{A7}$$

A combination of A and $F_{\rm Edd}$ gives a distance-independent quantity, the Eddington temperature:

$$T_{\rm Edd,\infty} = \left(\frac{gc}{\sigma_{\rm SB}\kappa_{\rm e}}\right)^{1/4}\frac{1}{1+z} = 1.14\times10^8\,A\,F_{-7}^{1/4}\ {\rm K}, \tag{A8}$$

where $F_{-7} = F_{\rm Edd}/10^{-7}$ erg cm^{-2} s^{-1}. This gives a parametric relation between radius and mass of the NS via compactness u:

$$R = \frac{c^3u(1-u)^{3/2}}{2\kappa_{\rm e}\sigma_{\rm SB}T_{\rm Edd,\infty}^4} = 1188\frac{u(1-u)^{3/2}}{(1+X)\,T_{\rm Edd,\infty,7}^4}\ {\rm km},$$
$$m \equiv \frac{M}{{\rm M}_\odot} = u\frac{R}{2.95\ {\rm km}}, \tag{A9}$$

where $T_{\rm Edd,\infty,7} = T_{\rm Edd,\infty}/10^7$ K. It is easy to see that for the same $T_{\rm Edd,\infty}$ and same compactness u, the NS radius is two times larger for helium model ($X = 0$) than for hydrogen model ($X = 1$).

Expression (A6) gives the basis for the cooling tail method (Suleimanov et al. 2011a,b). From the observations we obtain the relation between $K^{-1/4}$ and flux F, which is fitted with the theoretical dependence $Af_{\rm c}(F/F_{\rm Edd})$ with the free parameters being $F_{\rm Edd}$ and normalization A. This is different from the touchdown method that was used by Özel et al. (2009) and Güver et al. (2010a,b), who assume that the touchdown flux is equal to the Eddington flux, take some value for blackbody normalization K in the cooling tail and assume a value for $f_{\rm c}$. The cooling tail method uses the information from the whole cooling tail (not only two numbers), actually allows to check (e.g. in terms of χ^2) whether the spectral evolution in the cooling tail is consistent with the NS atmosphere models, does not require any assumption for the colour-correction factor in the cooling tail and is not based on the assumption of equality of the touchdown and the Eddington flux. Of course, the theoretical dependence of $f_{\rm c}$ still depends on the chemical composition of the atmosphere and the gravity. The gravity can be varied to get a self-consistent solution for the mass and radius.

Once A and $F_{\rm Edd}$ are known and some value for the distance is assumed, it is easy to compute the resulting NS mass and radius. Radius at infinity is found via equation (A7). From the Eddington flux, we can find the quantity

$$C = \frac{R_{\rm S}}{1+z} = 0.4\frac{F_{\rm Edd}D^2(1+X)}{c^3} = 14.1(1+X)D_{10}^2F_{-7}\ {\rm km}. \tag{A10}$$

Combining equations (A7) and (A10), we can define a dimensionless quantity

$$\alpha \equiv 4C/R_\infty = 4u(1-u) = 56.5(1+X)F_{-7}A^2D_{10}. \tag{A11}$$

Equation (A11) can be solved for u:

$$u = u_\pm = \frac{1}{2}\left(1\pm\sqrt{1-\alpha}\right). \tag{A12}$$

The solution exists only if $\alpha \le 1$, which can be translated to the upper limit on the distance

$$D_{10} \le D_{10,\max} = \frac{1.77\times10^{-2}}{(1+X)A^2F_{-7}} = 1.77\times10^{-2}\frac{K^{1/2}f_{\rm c}^2}{(1+X)F_{-7}}. \tag{A13}$$

Solutions (A12) can be rewritten for the redshift factor

$$(1+z)_- = \left(\frac{2}{1+\sqrt{1-\alpha}}\right)^{1/2}, \tag{A14}$$

$$(1+z)_+ = \frac{2}{\alpha^{1/2}}\left(\frac{1+\sqrt{1-\alpha}}{2}\right)^{1/2}. \quad \text{(A15)}$$

And finally the NS mass and radius can be obtained

$$m = \frac{C}{2.95\ \mathrm{km}}(1+z) = \alpha(1+z)\frac{R_\infty}{11.8\ \mathrm{km}},$$

$$R = R_\infty/(1+z). \quad \text{(A16)}$$

From given prior distributions of A, $F_{\rm Edd}$ and D, using equations (A10)–(A16) we can simulate the posterior distribution of M and R.

This paper has been typeset from a TEX/LATEX file prepared by the author.